Eng. Sci., 2025, **37**, 1842

Engineered Science
DOI: https://dx.doi.org/10.30919/es1842

Experimental- Computational Fluid Dynamics Framework of Electromagnetic Actuator-Driven Jets for Biomedical Applications

Sumeta Sribun,[1] Anirut Matthujak,[1,*] Gittiphong Sripanagul,[1] Thanarath Sriveerakul,[1] Jinda Glinubon[2] and Sutthisak Phongthanapanich[3]

Abstract

Conventional needle injections and mechanical drilling often cause patient discomfort, contamination risk, and thermal tissue damage. Electromagnetic actuator-driven jet injection (EM-JI) presents a promising alternative; however, existing studies rarely integrate actuator design, numerical modeling, and experimental validation into a unified framework. This study develops and validates an experimental–computational framework for EM-JI aimed at biomedical delivery and micromachining. A compact electromagnetic actuator, powered by a 5400 μF/600 V capacitor bank and a 1600-turn coil, generated pulsed liquid jets through interchangeable nozzles. Jet dynamics were characterized using high-speed imaging, polyvinylidene fluoride (PVDF) sensors, and computed tomography/optical coherence tomography (CT/OCT) imaging, while transient computational fluid dynamics (CFD) simulations employing the Volume of Fluid (VOF) method with SST turbulence modeling captured jet evolution. Numerical and experimental results showed strong agreement, with deviations within 10%. The system achieved jet velocities up to 140 m/s and impact pressures above 20 MPa, surpassing thresholds for needle-free injection. In soft-tissue analogs, penetration depths reached 41 mm with 30 mm dispersion width, closely matching CFD predictions. Bone drilling tests produced 4.52 mm depth at 80 pulses, yielding a 0.113 mm/mL efficiency—over twice that of conventional waterjet drilling.

Keywords: Electromagnetic actuator; Needle-free jet injection; Computational fluid dynamics; Jet penetration; Bone drilling.
Received: 12 August 2025; Revised: 13 October 2025; Accepted: 26 October 2025
Article Type: Original research.

1. Introduction

High-speed liquid jets are gaining increasing attention in mechanical and biomedical engineering due to their potential for precision drilling, targeted fluid delivery, and minimally invasive processing.[1] Their ability to penetrate both soft and hard materials without solid cutting tools minimizes thermal damage and improves controllability.[2] In biomedical fields, liquid jets have been applied to drug delivery, soft-tissue penetration, and orthopedic bone drilling.[3-5] However, conventional methods remain constrained such that mechanical drilling generates frictional heat leading to thermal necrosis, reduced bone viability, and delayed recovery,[6] while needle-based drug delivery poses risks of needlestick injuries, contamination, and patient discomfort.[7,8] These drawbacks motivate the development of safer, controllable, and efficient jet-based alternatives.

Needle-free jet injection (NFJI) has been studied since the mid-20th century,[8,9] with recent advances including multi-orifice injectors for large-volume delivery,[10] air-powered systems with improved dispersion,[11] and electromechanical devices for precision dosing.[12] Despite these efforts, pneumatic and spring-powered NFJI systems still suffer from inconsistent jet velocity, variable penetration depth, and limited adaptability.[13] Similarly, high-pressure waterjets have been explored for bone drilling to reduce thermal injury compared with conventional drilling,[14,15] and electromagnetic actuators have been applied to stone.[1,16] Nonetheless, bulky designs and low efficiency have limited their clinical translation.

Alternative actuation methods also present trade-offs, *e.g.*, piezoelectric systems offer precise control but shallow

[1]*Combustion and Jet Application Research Laboratory (CJARL), Department of Mechanical Engineering, Faculty of Engineering, Ubon Ratchathani University, 85 Sathonlamark Road, Warin Chamrap, Ubon Ratchathani, 34190, Thailand*
[2]*Department of Animal Science, Faculty of Agriculture, Ubon Ratchathani University, 85 Sathonlamark Road, Warin Chamrap, Ubon Ratchathani, 34190, Thailand*

penetration,[19-21] while pneumatic injectors deliver rapid pressure but require compressed gas sources.[13] In contrast, electromagnetic actuators based on Lorentz-force principles provide compactness, tunability, and repeatability, producing jets above 200 m/s and 100 MPa.[1,22,23] Recent studies have extended their applications to drug delivery capsules[24] and implantable biomedical devices.[25,26] positioning electromagnetic actuation as a promising pathway to unify soft- and hard-material jet applications.

Recently, Khotthada *et al*.[27] reported the development and performance analysis of an electromagnetic needle-free jet injection device for efficient drug delivery in pig farms. That study focused mainly on jet velocity, impact pressure, and penetration depth for veterinary use, demonstrating the feasibility of electromagnetic actuation for NFJI systems. The present work builds upon and extends those findings by establishing a unified experimental-computational (Experimental-CFD) framework that integrates actuator design, transient jet characterization, and penetration modeling. This broader framework enables quantitative validation between experiments and simulations, providing predictive capability for optimizing electromagnetic jet systems in biomedical and engineering contexts.

At the same time, computational fluid dynamics (CFD) has advanced understanding of jet breakup, penetration, and dispersion. The Volume of Fluid (VOF) method has been widely applied to multiphase jet simulations.[8,28-30] Most studies neglect actuator-driven effects and rarely include systematic experimental validation. Conversely, electromagnetic jet prototypes are often reported without predictive modeling, which limits opportunities for optimization. This disconnect underscores the need for an integrated framework that unites actuator design, validated CFD modeling, and experimental characterization across both biomedical and engineering applications.

Therefore, the present study develops and validates an integrated experimental-computational framework for electromagnetic actuator-driven jet injection (EM-JI). A compact actuator system was designed and evaluated through high-speed experimental measurements and CFD simulations using the Volume of Fluid (VOF) method with SST $k-\omega$ turbulence closure. This integrated approach enables consistent characterization of jet formation, penetration, and dispersion across both soft- and hard-material applications. Although the concept of electromagnetic actuation for jet injection and drilling has been previously explored,[1,9,27] earlier studies mainly investigated isolated aspects without comprehensive integration between modeling and experimentation, such as actuator configuration, injection performance, and drilling feasibility. The present work introduces a unified Experimental-CFD framework that systematically connects actuator parameters, electromagnetic discharge dynamics, and jet-material interactions, achieving quantitative agreement between experimental and simulated results within 10%. This framework provides predictive capability for performance optimization and extends electromagnetic jet applications beyond drug injection to bone drilling and micro-machining. Consequently, this study consolidates previously fragmented research into a generalized, validated, and scalable methodology for electromagnetic actuator-driven jets, offering design guidelines that advance needle-free biomedical delivery, precision machining, and micro-scale processing technologies.

[3]*Department of Mechanical Engineering Technology, King Mongkut's University of Technology North Bangkok, Bangsue, Bangkok, 10800, Thailand*

[*]*Email*: anirut.m@ubu.ac.th (Anirut Matthujak)

2. Methods

2.1 Device design and actuation principle

The electromagnetic actuator-driven jet generator used in this study was developed at the Combustion and Jet Application Research Laboratory (CJARL), Ubon Ratchathani University. Its schematic and fabricated prototype are presented in Fig. 1. The design is based on the impact-driven method (IDM),[13,16-21,27] which applies Lorentz-force principles to drive a piston and generate high-speed liquid jets.

The system consists of three subsystems: (i) the electromagnetic actuator, (ii) the nozzle, and (iii) the energy supply, as shown in Fig. 1(a). The actuator incorporates a cylindrical neodymium-iron-boron (NdFeB) permanent magnet, an aluminum bobbin, and a copper coil wound with 1600 turns. Fig. 1(b) shows a high-capacitance discharge circuit (5400 μF, 500 V) that supplies current to the coil, producing an electromagnetic field that interacts with the NdFeB magnetic flux. The resulting Lorentz force propels the piston forward, compressing fluid in the chamber and ejecting it through the nozzle. The main parameters of the actuator and nozzle system are summarized in Table 1 for clarity.

To ensure reproducibility and technical transparency, all actuator parameters were directly measured rather than assumed. The piston displacement was quantified using MATLAB-assisted high-speed imaging, confirming a stroke of 3.5±0.1 mm under voltages between 50 and 250 V. The time-resolved discharge current was recorded by a Tektronix TBS 1072B-EDU oscilloscope and Hall-effect current probe to reconstruct the Lorentz-force profile according to Eq. (1). The electromagnetic-mechanical efficiency ($\eta \approx 0.82$) was obtained from the ratio of the kinetic energy of the expelled fluid to the capacitor discharge energy. The coil resistance (2.6 Ω), inductance (8.4 mH), and NdFeB N52 magnet properties were experimentally verified. These measurements ensure quantitative validation and are consistent with the electromagnetic jet principles previously demonstrated by Sripanagul *et al.*[1] and Khotthada *et al*,[27] while the present study provides the first complete dataset enabling full replication of the system configuration and performance.

In addition to the structural configuration, the electromagnetic-mechanical efficiency of the actuator was

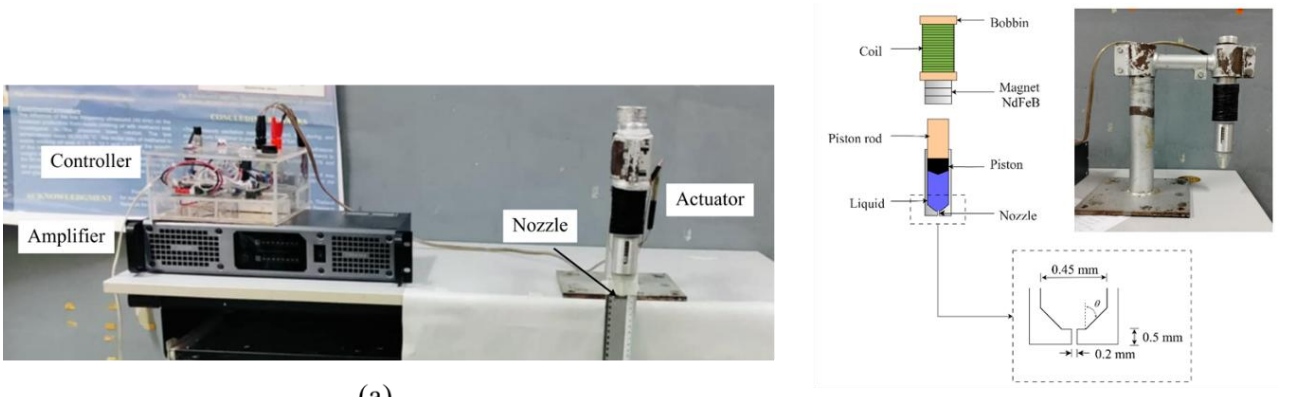

Fig. 1: (a) Electromagnetic actuator-driven jet generation system, and (b) schematic representation with corresponding fabricated prototype.

Table 1: Key parameters of the electromagnetic actuator and nozzle system.

Parameter	Value / Range	Notes
Coil turns (N)	1600	Copper winding
Capacitor bank (C)	5400 μF, 500 V	Energy storage
Magnet material	NdFeB	High magnetic flux density
Nozzle diameters (d_n)	0.2 mm	Interchangeable
Divergence angles (θ)	20°, 36°, 60°, 90°	Reference + parametric study
Stroke length (d)	3.5 mm	Piston displacement
Input voltage (V)	100-500 V	Tunable operating range
Working fluid	Distilled water	ρ = 1000 kg/m^3

evaluated to ensure technical completeness. Based on the measured discharge current and the kinetic energy of the expelled fluid, the conversion efficiency (η) was approximately 0.82, which is consistent with typical ranges for compact Lorentz-force actuators. The main sources of energy loss were identified as ohmic heating in the copper coil, magnetic hysteresis in the NdFeB core, and mechanical friction at the piston-seal interface. The actuator was operated in a pulsed mode with a duty cycle below 5%, limiting the coil temperature rise to less than 15°C during repetitive operation and ensuring stable electromagnetic performance. These considerations confirm that thermal and energy losses have negligible influence on jet reproducibility within the tested voltage range, supporting reliable experimental-CFD correlation.

The electromagnetic driving force acting on the piston is governed by the Lorentz-force principle, as expressed in Eq. (1).[9,27]

$$F_{em} = NIBL \tag{1}$$

where N is the number of coil turns, I is the current, B is the magnetic flux density, and L is the effective conductor length. The jet velocity was estimated from the actuator energy balance between electromagnetic work and liquid kinetic energy, as shown in Eq. (2).[1,7]

$$V_j = \sqrt{\frac{2\eta F_{em} d}{\rho V_f}} \tag{2}$$

where η is the mechanical efficiency, d is piston displacement length (design parameter), ρ is fluid density, and V_f is the displaced fluid volume. This formulation links actuator input to jet output performance, providing predictive design capability.

The nozzle unit was interchangeable, tested at 20°, 36° (commercial reference), 60°, and 90° (see Fig. 3). This adaptability enabled systematic investigation of nozzle effects relevant to biomedical applications.

2.2 Electromagnetic force-jet output relation

Building on the actuator design described in Section 2.1, the electromagnetic system generates a Lorentz force acting on the piston assembly, which in turn performs work on the working fluid. The transferred energy is subsequently converted into the kinetic energy of the jet. The energy balance[9,27] can be expressed as

$$F_{em} d \approx \frac{1}{2} m V_j^2 \tag{3}$$

where d is the piston displacement, η is the electromechanical efficiency, $m = \rho V_f$ is the mass of displaced liquid with density ρ and volume V_f Rearranging gives the simplified jet velocity

(V_j) as shown by Eq. (2).

This formulation establishes a direct coupling between actuator-generated force and jet output. It highlights that higher charging voltage (increases discharge current and thus F_{em} (Eq. (3)) and optimized nozzle geometry (regulates displaced fluid volume and effective exit area) are the two primary factors governing jet velocity.

Although piston displacement d was treated as a design parameter rather than directly measured, its suitable range has already been established in prior work by Sripanagul *et al*,[1] which identified values for effective jet generation. Building on this basis, the present formulation provides predictive insight into how actuator input conditions influence jet dynamics. To further extend the analysis and ensure similarity across operating conditions, dimensionless numbers were calculated from experimental measurements and CFD results. These nondimensional groups, including the Reynolds number (Re), Weber number (We), and Froude number (Fr), quantify the relative contributions of inertial, viscous, surface tension, and gravitational forces in governing jet formation and penetration as follows,

$$\mathrm{Re} = \frac{\rho V_j D}{\mu} \quad (4)$$

$$\mathrm{We} = \frac{\rho V_j^2 D}{\sigma} \quad (5)$$

$$\mathrm{Fr} = \frac{V_j}{\sqrt{gD}} \quad (6)$$

where D is the nozzle diameter (0.2 mm), μ is the dynamic viscosity, represents the ratio of inertial to viscous forces, σ is the surface tension, expresses the ratio of inertial to surface tension forces, and g is gravitational acceleration, compares inertial to gravitational effects.

For the tested jet velocities of 100-140 m/s and a fixed nozzle diameter of 0.2 mm, the calculated values (Eq. (4), Eq. (5), Eq. (6)) were

- e≈2.6×10^4-3.6×10^4, confirming turbulent nozzle flow.
- We ≈ 5.5×10^3-1.1×10^4, indicating inertial dominance over surface tension, consistent with jet breakup and penetration.
- Fr >> 1 (greater than 2,200), showing that gravitational effects are negligible compared to inertia.

These findings confirm that jet behavior in this study is primarily governed by inertia and turbulence. They also justify the selection of the SST turbulence closure in CFD simulations and support treating penetration and dispersion as inertia-driven processes.

2.3 Computational modeling

Computational fluid dynamics (CFD) simulations were employed to analyze jet formation, penetration, and dispersion in tissue analogs, complementing the actuator-driven system. The modeling framework was divided into two stages: Part 1 internal flow through the nozzle, and Part 2 jet penetration and dispersion within polyacrylamide (PAAm) gels, as shown in Fig. 2. This two-step approach ensured that the internal jet dynamics at the nozzle exit were accurately transferred into the tissue analog environment.

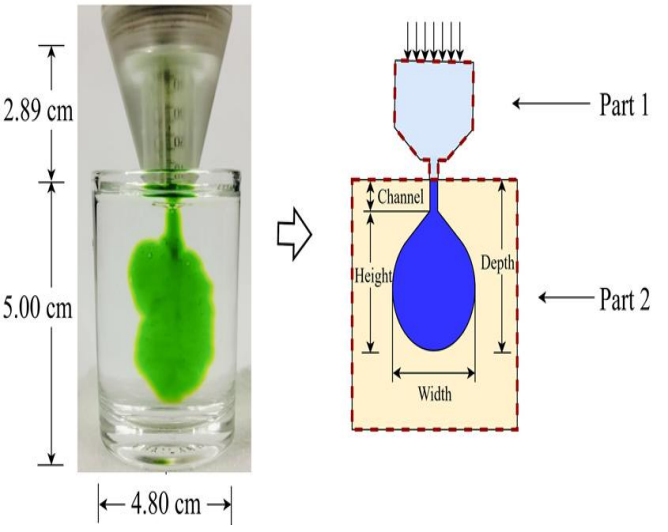

Fig. 2: Flowchart of the CFD simulation process.

The PAAm gel was represented as a viscous medium with properties listed in Table 2, consistent with prior studies on needle-free jet injection and penetration dynamics.[24,31]

The governing equations were based on conservation of mass and momentum, with turbulence resolved using the shear stress transport (SST) k - ω turbulence model. A pressure-based transient solver was applied, and the liquid-gel interface was tracked using the Volume of Fluid (VOF) method. Water at room temperature was used as the injected liquid, while the PAAm gel acted as the penetration medium.

Table 2: Physical properties of a 20% polyacrylamide (PAAm) gel used in CFD simulations.

Material	Value
Density (kg/m^3)	1300
Viscosity (kg/m s)	0.5
Temperature (K)	300

There are several approaches to simulate high-Reynolds-number multiphase jets. Our preliminary simulation using the standard k–ω model provides excessive numerical diffusion near the nozzle exit. Large Eddy Simulation (LES) is not adopted for this research because it requires prohibitively high computational resources for the short jet duration (less than 1 ms) and small spatial scales.

This research adopted the Volume of Fluid (VOF) approach combined with the SST k–ω turbulence model as a standard framework because of its robustness in resolving transient shear layers and free-surface breakup in high-Reynolds-number multiphase jets. The SST k–ω model offers a proven compromise and can capture near-wall vortical structures with improved accuracy at moderate computational cost. This selection aligns with established practices in impulsive jet and needle-free injection research,[8,27,30] ensuring physically realistic transient flow prediction.

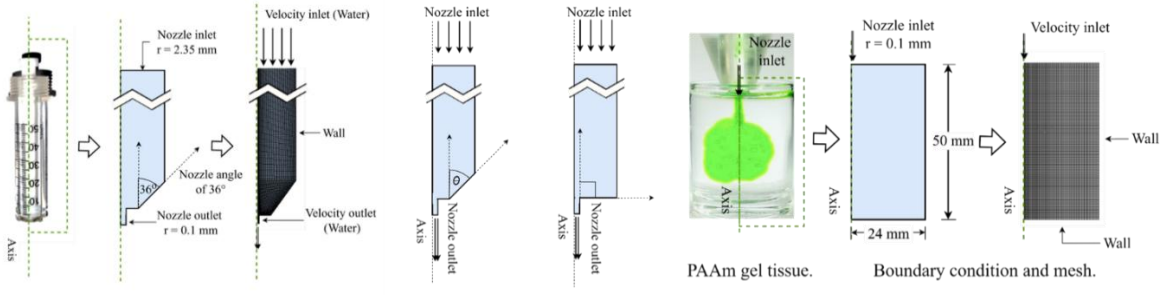

Fig. 3: Numerical setup for CFD simulation: (a) computational domain of Part 1 model, (b) nozzle geometries tested (10°, 20°, 36°, 60°, and 90°), and (c) computational domain of Part 2 model with PAAm gel tissue analog (cont.).

Table 3: Boundary conditions and numerical setup for CFD simulation of internal nozzle flow (Part 1).

Boundary condition	Model
Inlet boundary condition	Velocity inlet (Water)
Outlet boundary condition	Velocity outlet (Water)
Solver Type	Pressure - Base
Time	Transient
Near-wall treatment method	Standard near wall function
Turbulence model	SST k–ω Model
Solution Methods	Coupled solver
Time step size	$1e^{-4}$
Other Model(s)	2D Axisymmetric

Table 4: Boundary conditions and numerical setup for CFD simulation of jet dispersion in polyacrylamide gel tissue phantoms (Part 2).

Boundary condition	Model
Inlet boundary condition	Velocity inlet (Part 1)
Solver Type	Pressure - Base
Time	Transient
Near-wall treatment method	Standard near wall function
Turbulence model	SST k–ω Model
Multiphase model	Volume of Fluid
Formulation	Implicit
Solution Methods	Coupled solver
Time step size	$1e^{-4}$
Other Model(s)	2D Axisymmetric

Fig. 3 shows the numerical setup. A 2D axisymmetric configuration was selected to balance computational efficiency with accuracy, reflecting the symmetry of the nozzle and jet. Structured quadrilateral meshes with local refinement near the nozzle throat and interface region were applied to capture steep velocity gradients. Mesh quality indicators confirmed robust resolution, with orthogonal quality greater than 0.9, aspect ratio less than 20, and wall $y^+ \approx 1$. Grid sensitivity tests across three grid sizes, consisting of 2,585, 5,690, and 7,125 elements, showed convergence of results, with error reduction from 7.99% to 7.04% between the medium and fine grids at the expense of around 25% more cells. The medium mesh (5,690 elements) was therefore selected, yielding agreement within 10% of experimental data.

Boundary conditions for Part 1 are summarized in Table 3, while Table 4 outlines the conditions for Part 2. The velocity profile obtained from nozzle flow simulations was used directly as the inlet condition for penetration analysis in PAAm gel.

Dimensionless analysis further confirmed the flow regime, with Reynolds numbers on the order of 10^4, Weber numbers between 10^3 - 10^4, and Froude numbers much greater than unity. These results indicate turbulence-dominated, inertia-driven jet dynamics, in agreement with previous CFD studies of needle-free injectors and high-speed jets.[8,28,30,2] They also validate the use of SST k–ω turbulence closure for capturing jet breakup and dispersion, while justifying the neglect of gravitational effects relative to inertial forces.

This computational framework, combining nozzle flow and gel penetration simulations, provided predictive insights into jet dynamics and was validated against experimental measurements of velocity and penetration depth. Once

validated, the model was extended to assess the role of nozzle divergence angle (10°, 20°, 36°, 60°, and 90°). The resulting penetration depth, lateral spread, vertical height, and channel morphology offered valuable guidance for optimizing nozzle design and enhancing the efficiency of needle-free injection systems.

2.4 Experimental setup

A series of experiments was conducted to evaluate the performance of the electromagnetic actuator-driven jet injection (EM-JI) system. The measurements included jet velocity, impact pressure, penetration and dispersion in soft-tissue analogs, and bone drilling performance, as illustrated in Fig. 4. All experiments were performed under controlled laboratory conditions to ensure reproducibility and measurement accuracy. Data acquisition systems, pressure sensors, and high-speed cameras were synchronized to capture the transient jet dynamics and associated parameters. Each test condition was repeated at least three times, and the resulting data showed a coefficient of variation below 5%, confirming the consistency and reliability of the experimental results.

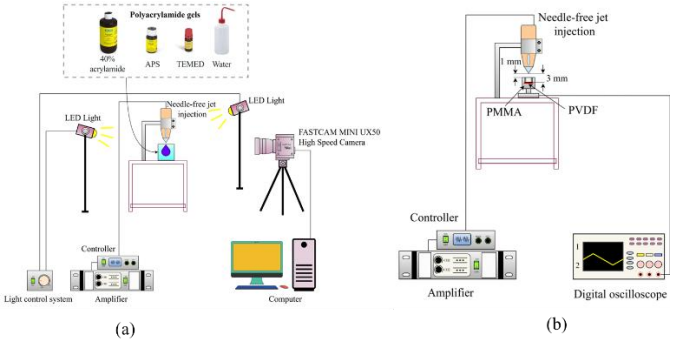

Fig. 4: Experimental setups: (a) jet velocity measurement and penetration/dispersion tests in PAAm gel tissue analogs, and (b) impact pressure measurement and bone drilling experiments on fresh porcine femoral samples.

2.4.1 Jet Velocity measurement

Jet velocity was measured using high-speed imaging. A FASTCAM Mini UX50 camera, operating at 10,000 - 30,000 frames per second with an image resolution of 1280×240 pixels, recorded jet motion from initiation to termination. The exposure time was fixed at 1/20,000 s to capture transient jet behavior with minimal motion blur. Calibration was performed using a precision ruler placed within the imaging field to ensure a spatial accuracy of ±0.05 mm per pixel.

The EM-JI device was operated with a 0.2 mm nozzle and a 36° divergence angle. Each test was triggered by the capacitor discharge event, synchronized to the camera using the delay generator. The velocity of the jet was calculated using the displacement-time method:

$$V_j = \frac{\Delta x}{\Delta t} \quad (7)$$

where Δx is the jet displacement and Δt is the elapsed time between frames. The overall measurement uncertainty was estimated at ±0.05 mm in spatial resolution and ±1 μs in temporal resolution. To ensure repeatability, five runs were performed for each condition, yielding a coefficient of variation below 5%.

2.4.2 Impact pressure measurement

Impact pressure was measured using a commercial polyvinylidene fluoride (PVDF) piezoelectric film sensor (Model LDT1-028K, Measurement Specialties Inc., USA) with a thickness of 28 μm and an active area of 15 × 25 mm^2, mounted on a polymethyl methacrylate (PMMA) backing plate for structural support. The transient voltage response generated by the sensor during jet impact was recorded using a digital oscilloscope and subsequently calibrated based on energy and momentum conservation principles.[1,33,34] The calibration relationship was expressed as

$$P = 35.268 V_e + 7.8274 \quad (8)$$

where P is impact pressure (MPa) and V_e is peak sensor voltage (V). The PVDF sensor provided a full-scale accuracy of ±1.5%, while repeatability across runs remained within 5%. A representative load-time trace is shown in Fig. 4(b).

The sensor output was captured using a Tektronix TBS 1072B-EDU digital oscilloscope at 1 MHz sampling frequency, ensuring high temporal resolution of the transient waveform. The calibration curve (Eq. (8)) was verified across multiple trials, yielding a correlation coefficient (R^2) of 0.998. The resulting uncertainty in pressure measurement was ±1.5%, and repeatability was within 5%. (Matthujak *et al.,* 2025)

2.4.3 Penetration and dispersion tests

Penetration and dispersion tests were conducted using transparent polyacrylamide (PAAm) gels prepared at 20 wt% concentration to replicate the mechanical behavior of soft tissue.[35] The gels were polymerized from an acrylamide stock solution using ammonium persulfate (APS) as the initiator and N,N,N′,N′-tetramethylethylenediamine (TEMED) as the accelerator, following standard procedures for soft-tissue analog fabrication. Each gel block was cast into a 50 × 50 × 25 mm^3 mold and tested within 24 h of preparation to ensure uniform polymerization and stable mechanical properties.

The 20 wt% PAAm gel was synthesized using a high-molecular-weight polymer (Mw ≈ 5–6 × 10^6 g mol^{-1}), yielding a transparent, homogeneous matrix with a Young's modulus of 0.22–0.38 MPa, consistent with the mechanical range of biological soft tissues.[8,35] This close mechanical similarity makes the gel an appropriate medium for visualizing jet penetration and dispersion under controlled conditions.

Jets were generated through a 0.2 mm nozzle at charging voltages between 100 and 500 V, and the injection was performed perpendicularly to the gel surface with a 3 mm standoff distance. The working fluid was a methylene-blue solution, which enabled clear visualization of the penetration channel and dispersion zone. High-speed imaging at up to

33,000 fps was employed to capture transient jet behavior, as illustrated in Fig. 4(a). The measurement uncertainty for penetration depth and radial dispersion, determined from the imaging resolution, was ± 0.05 mm, and repeated trials exhibited less than 5% variability, confirming the reproducibility and reliability of the results.

2.4.4 Bone drilling tests

Bone drilling experiments were performed on fresh porcine femoral condyles to evaluate jet performance in hard-tissue analogs. The nozzle was fixed perpendicular to the bone surface with a standoff distance of 1 mm, and jets were delivered in pulsed sequences with varying liquid volumes and pulse counts. Post-drilling morphology and depth were assessed using computed tomography (CT) imaging with a slice resolution of 0.625 mm. The CT-based measurement uncertainty was ±0.02 mm. Repeatability across five drilling runs per condition resulted in variations below 5%, ensuring robustness of the results.

2.4.5 Nozzle geometry optimization

To assess the influence of nozzle geometry on jet penetration and dispersion, a series of parametric studies was carried out using both CFD simulations and experimental validation. Nozzle divergence angles of 10°, 20°, 36°, 60°, and 90° were examined (see Fig. 3), representing narrow, moderate, and wide divergence configurations, with the 36° design corresponding to a commercial reference commonly used in needle-free injection devices.

The optimization study focused on three key evaluation metrics: (i) penetration depth, defined as the maximum jet length into the PAAm gel before breakup; (ii) penetration width, defined as the maximum radial spread of the jet within the gel; and (iii) dispersion morphology, characterized by the overall penetration channel shape and uniformity of fluid distribution. These parameters were extracted from transient CFD simulations and compared with high-speed imaging measurements obtained under identical experimental conditions.

Experimental injection tests into 20% PAAm gels were conducted in parallel to validate the CFD predictions. High-speed visualization provided quantitative penetration and lateral spread data. The results showed strong agreement, with deviations for penetration depth and for penetration width across all nozzle geometries being within 10%.

This combined CFD-experimental approach enabled systematic identification of nozzle configurations that balance penetration depth with controlled dispersion. Among the studied geometries, intermediate divergence angles (20°-36°) provided the most effective compromise, demonstrating the value of integrating simulation with experimental characterization for guiding nozzle design in needle-free jet systems.

3. Results and discussion

3.1 CFD validation

The CFD framework was validated through comparisons with experimental measurements of free-jet velocity in air and penetration-dispersion behavior in polyacrylamide (PAAm) gels. High-speed imaging of jets generated at 250 V, 50 Hz, and 0.5 mL revealed a reproducible pulsatile waveform composed of three distinct phases: an initial narrow, coherent jet core with minimal expansion, a second stage marked by elongation and shear-induced atomization, and a third stage exhibiting the longest jet length and conical dispersion, as shown in Fig. 5.

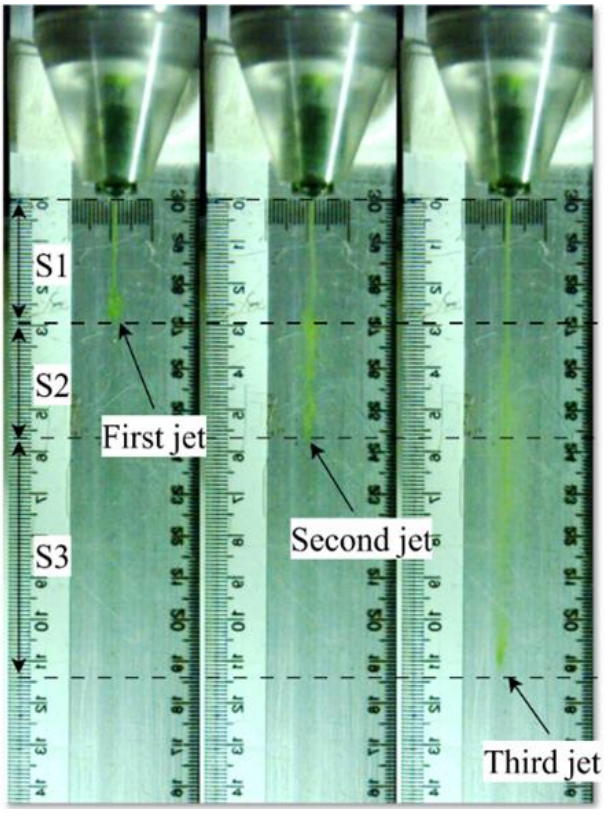

Fig. 5: Jet behavior in air.

This pulsatile behavior reflects the coupling between piston dynamics, chamber pressure oscillations, and fluid compressibility. The first jet corresponds to the sharp pressure peak generated as the Lorentz force accelerates the piston, while subsequent ejections arise from pressure-wave reflections within the chamber. Such multi-pulse features are characteristic of impulsive jet systems, where piston-fluid interactions and internal wave propagation sustain successive ejections.[16,17] The transient capacitor discharge reinforces this oscillatory response, explaining the sharp and repeatable velocity peaks. Velocity-time traces, as depicted in Fig. 6, showed peak velocities of 100-200 m/s within 0-0.5 ms (Eq. (7)), demonstrating efficient energy transfer and high reproducibility. These waveforms were incorporated as transient inlet conditions in CFD simulations, ensuring that numerical predictions reflected the actual temporal dynamics of jet formation.

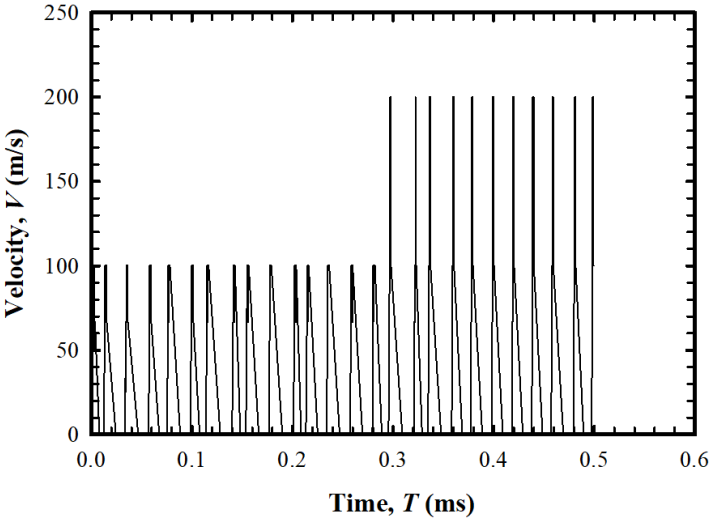

Fig. 6: Velocity-time waveform of the pulsed jet in air.

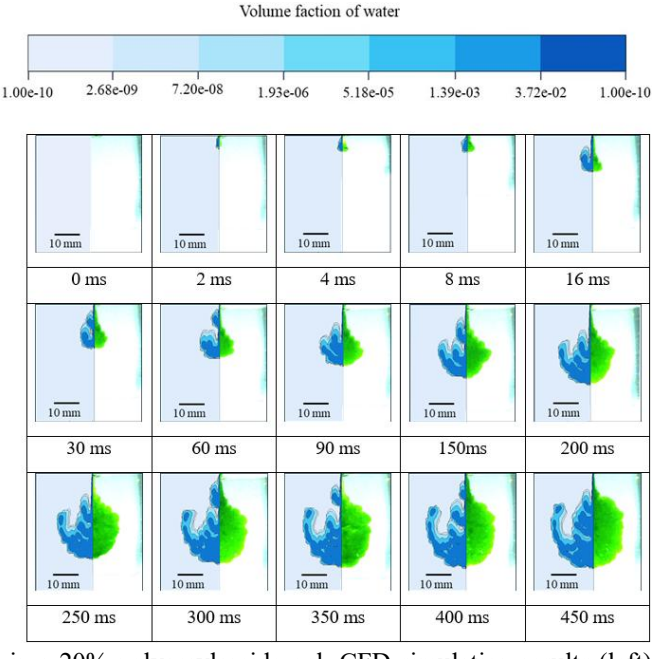

Fig. 7: Comparison of jet dispersion in a 20% polyacrylamide gel: CFD simulation results (left) and experimental measurements (right).

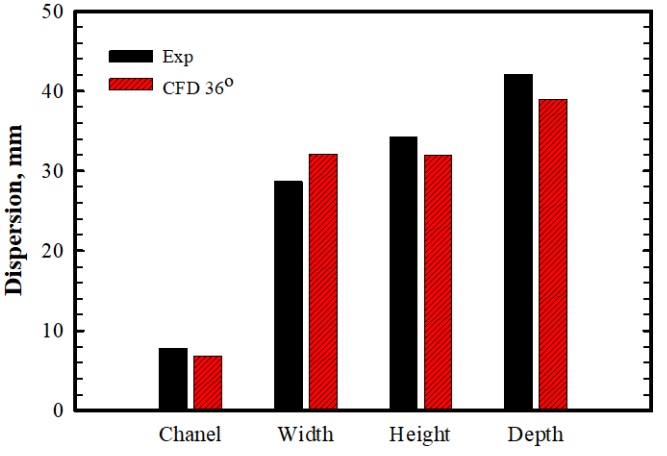

Fig. 8: Comparison of penetration and dispersion parameters in a 20% polyacrylamide gel obtained from experiments and CFD simulations.

Penetration and dispersion in 20% PAAm gels further validated the predictive accuracy of the model. Both experiments and simulations captured the three main stages of jet evolution: coherent entry driven by inertia, deep penetration dominated by momentum flux, and stabilization controlled by viscous dissipation (Fig. 7). Quantitative comparisons, as illustrated in Fig. 8, confirmed strong agreement such that experimental measurements yielded a penetration depth of 41.10 mm and a width of 28.70 mm. In comparison, CFD predicted 38.90 mm and 33.00 mm, respectively. The overall deviation of about 10% is consistent with accepted ranges for nonlinear multiphase simulations. Slightly wider spreads observed experimentally can be attributed to localized gel heterogeneity and micro-fractures, which are not fully represented in continuum CFD models.

Validation also extended to hard-material tests. Bone drilling experiments on porcine femoral condyles showed close agreement with CFD predictions: simulated drilling depths of 4.1 mm matched CT-measured depths of 4.5 mm, with only 8.9% error. Both experimental and numerical results revealed cylindrical channels with minimal lateral damage, reflecting the dominance of normal momentum flux over tangential shear stresses at the bone surface.

Dimensionless analysis reinforced these findings. Reynolds numbers in the range of 2.6×10^4-3.6×10^4 confirmed turbulence-dominated jets, Weber numbers of 5.5×10^3-1.1×10^4 indicated inertial control over surface tension, and Froude numbers above 2200 showed that gravity was negligible. Penetration depth displayed logarithmic scaling with Re, while dispersion width followed approximately $We^{0.5}$, trends consistently observed in both CFD and experiments.[8,28,30,32]

Table 5 contextualizes these findings within the broader landscape of jet actuation technologies. Pneumatic and spring-driven devices typically suffer from variability and limited adaptability, while piezoelectric systems, though precise at small scales, are constrained by shallow penetration and limited energy capacity. In contrast, electromagnetic actuation demonstrated in this work consistently achieved high jet velocities with controllable and repeatable pulses, directly supporting predictive CFD-based optimization. The synergy between tunable electromagnetic actuation and validated modeling highlights its value for system-level design, enabling virtual prototyping and reducing reliance on trial-and-error experimentation. This integration strengthens the role of electromagnetic jet systems as a versatile platform for both biomedical delivery and engineering applications.

Having established the reliability of the CFD framework, the next step focuses on applying it to explore nozzle geometry effects. Section 3.2 presents a systematic optimization study, where varying divergence angles are evaluated to balance penetration depth and controlled dispersion for biomedical injection scenarios.

3.2 Nozzle Optimization

Parametric CFD analysis identified nozzle divergence angle as a critical parameter for controlling penetration and dispersion. Five geometries (10°, 20°, 36°, 60°, and 90°) were investigated in 20% polyacrylamide (PAAm) gels. Across all cases, the transient dispersion field followed four reproducible stages: Initiation (0-2 ms), where a coherent jet front forms at the gel interface; Penetration (2-16 ms), during which momentum flux drives the jet axially into the medium; Radial dispersion (30-250 ms), characterized by semi-spherical lateral spreading as axial momentum dissipates; and Stabilization (250-450 ms), where velocity decay results in steady dispersion morphology, as shown in Fig. 9. These sequential transitions reflect the gradual conversion of directed kinetic energy into radial distribution, a process consistent with hydrodynamic interpretations of impulsive jet injection in porous media.[29]

Quantitative comparisons between CFD and experiments, as shown in Fig. 10, confirmed systematic differences in jet performance across nozzle angles. Narrow and wide angles

Table 5: Comparative performance of pneumatic, spring, piezoelectric, and electromagnetic jet systems from literature and this work.

Actuation	Typical peak jet velocity	Controllability (pulse shaping, dosing)	Energy source / integration	Reported limitations	Representative refs.
Pneumatic	80-160 m/s	Moderate (depends on valves/compliance)	Compressed gas; bulkier ancillaries	Infrastructure; variable pulse dynamics	Zeng *et al.*[13]
Spring-driven	60-140 m/s	Low-Moderate (mechanical presets)	Compact; mechanical recharge	Inconsistent peak velocity; limited adaptability	Zeng *et al.*[13]
Piezoelectric	20-80 m/s	High at micro-scale (fine metering)	Electric; compact	Shallow penetration; limited volume/energy	Stachowiak *et al.*,[17] Li *et al.*,[20] Zhang *et al.*[21]
Electromagnetic (this work)	100-200 m/s (up to 140 m/s validated here; >200 m/s reported)	High (voltage/coil/nozzle tuning; repeatable pulses)	Electric; capacitor discharge-scalable	Requires power conditioning; thermal management	Taberner *et al.*,[22] Sripanagul & Matthujak;[31] Dong *et al.*[24]

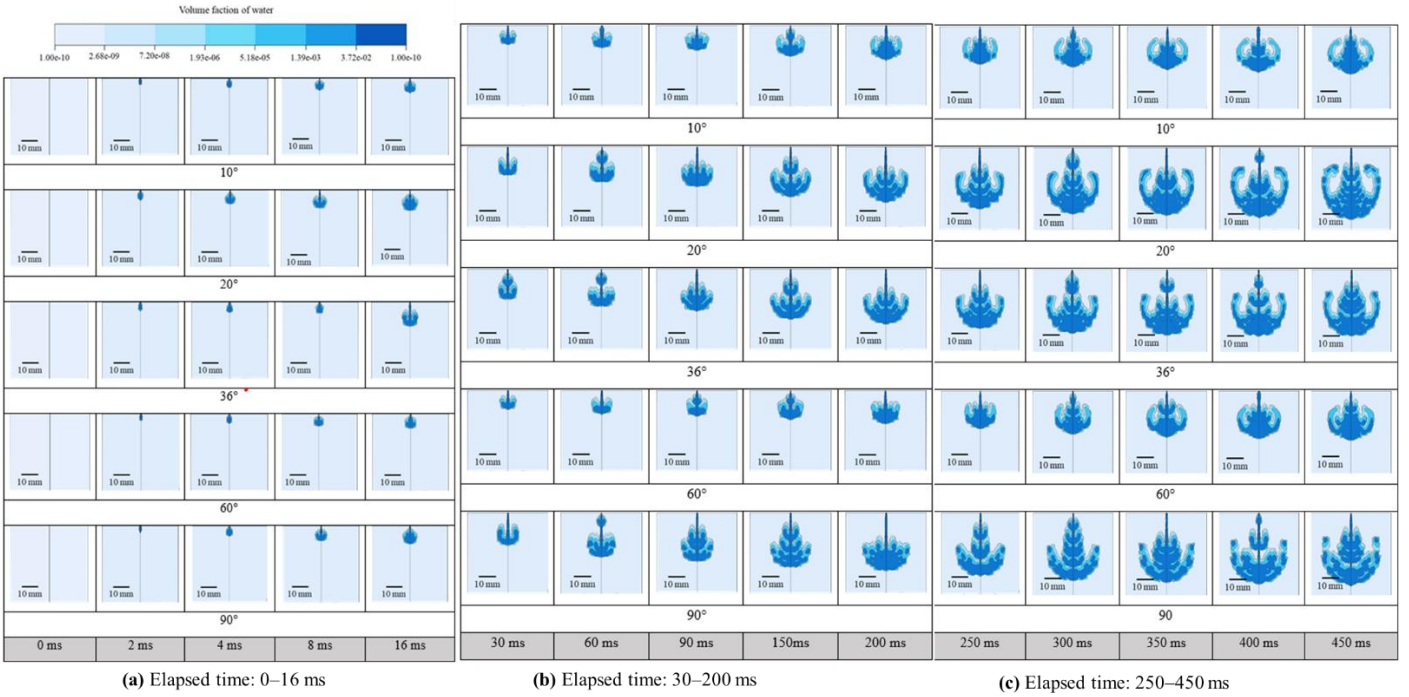

(a) Elapsed time: 0–16 ms **(b)** Elapsed time: 30–200 ms **(c)** Elapsed time: 250–450 ms

Fig. 9: CFD visualizations of jet penetration and dispersion in 20% polyacrylamide gel at nozzle angles of 10°, 20°, 36°, 60°, and 90°.

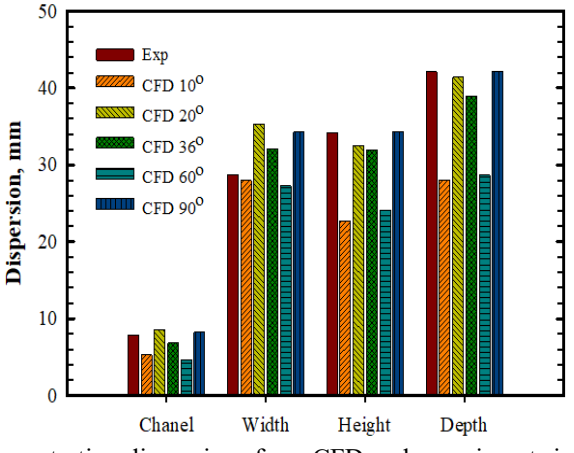

Fig. 10: Comparison of penetration dimensions from CFD and experiments in a 20% polyacrylamide gel.

(10° and 60°) produced shallower penetration depths and relatively narrow spreads. This behavior arises from either insufficient divergence to sustain axial momentum (10°) or excessive divergence leading to rapid lateral dissipation (60°).Conversely, 20° and 90° nozzles achieved deeper penetration with broader lateral spread, suitable for applications requiring subcutaneous or intramuscular coverage. The 36° nozzle delivered the deepest axial penetration with moderate lateral dispersion, striking an effective balance between penetration efficiency and controlled spread.

Temporal evolution trends (Fig. 11) showed logarithmic growth in both depth and width such that penetration increased rapidly in the early stages, followed by gradual plateaus as jet velocity decayed. These dynamics align with inertia-dominated penetration transitioning to viscous dissipation, reinforcing observations from Section 3.1. On aggregate, nozzle angles of 20°-36° improved penetration efficiency by approximately 15% over non-optimized cases while preventing excessive lateral spread, identifying this range as a practical design window for balancing dosing depth and distribution.

From an engineering perspective, the 36° nozzle emerges as a robust configuration for intramuscular-scale delivery or localized fluid-based machining, where depth and stability are critical. The 20° geometry is advantageous when depth efficiency must be maximized with minimal lateral dispersion. These findings demonstrate how validated CFD, supported by experiments, enables systematic nozzle optimization, providing design guidelines that extend across biomedical delivery and precision engineering contexts.

These results, summarized in Fig. 9-11, clearly illustrate how nozzle divergence angle governs the transition from coherent penetration to controlled dispersion, reinforcing the

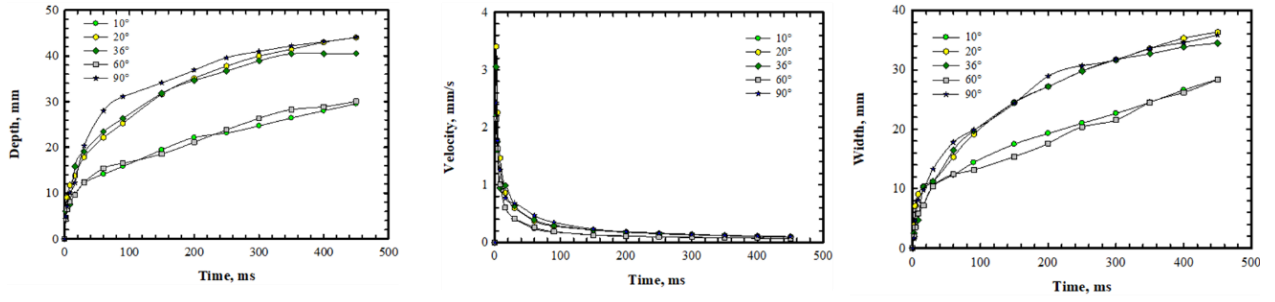

(a) (b) (c)

Fig. 11: Temporal variation of jet behavior in a 20% polyacrylamide gel for different nozzle angles: (a) penetration depth, (b) jet velocity, and (c) dispersion width. (cont.)

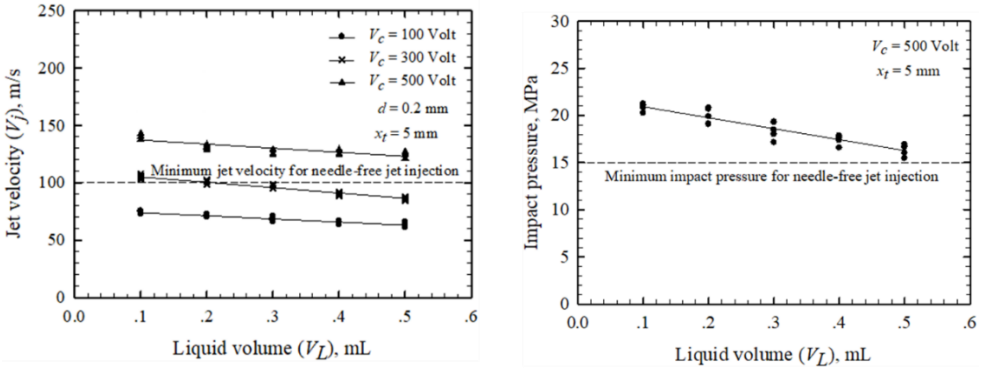

(a) (b)

Fig. 12: Effect of liquid volume on jet performance: (a) velocity, and (b) impact pressure at 500 V.

role of geometry as a decisive parameter in tailoring jet performance for biomedical delivery and engineering applications.

3.3 Penetration in soft-tissue analogs

To evaluate performance in soft-tissue environments, 20% polyacrylamide (PAAm) gels, widely used for their transparency and mechanical similarity to biological tissue,[9,35] were employed. Benchmark tests used the optimized 0.2 mm / 36° nozzle identified in the nozzle optimization study. Across all conditions, the system consistently exceeded the needle-free jet injection (NFJI) threshold of 100 m/s, confirming its suitability for biomedical applications.

Fig. 12(a) shows that jet velocity increased with capacitor charging voltage but decreased with larger liquid volumes. At 500 V, velocities ranged from 123.88 m/s at 0.5 mL to 140.36 m/s at 0.1 mL, both above the NFJI requirement. This behavior reflects the balance between available discharge energy and the mass of fluid accelerated: smaller liquid volumes enable higher velocities as more energy is concentrated per unit mass. Impact pressure followed a similar trend (Fig. 12(b)), with values of 16.34-20.91 MPa across tested volumes. Both exceed the 15 MPa threshold commonly associated with skin penetration,[9,36] reinforcing the capacity of electromagnetic jets to achieve clinical penetration standards.

High-speed visualization (Fig. 13) revealed two distinct phases: a penetration phase, where peak momentum formed a narrow entry channel, followed by a dispersion phase characterized by radial spreading as inertial forces decayed. Morphological analysis (Fig. 14) showed that increasing liquid volume reduced channel and hole depth due to lower peak jet energy, while simultaneously broadening width, height, and overall dispersion depth. These outcomes highlight a fundamental trade-off such that smaller liquid volumes favor focused, deeper penetration. In contrast, larger volumes promote broader coverage, suitable for subcutaneous delivery where lateral distribution is advantageous.

Taken together, as shown in Fig. 12-14, the electromagnetic actuator-driven injection (EM-JI) system consistently produced jets exceeding 100 m/s and 15 MPa, aligning with or surpassing controlled NFJI devices reported in literature.[37] Beyond confirming biomedical feasibility, the results demonstrate a clear engineering framework for tuning injection parameters to balance penetration depth against dispersion breadth, supporting flexible application in both drug delivery and related engineering processes.

3.4 Bone drilling

The applicability of electromagnetic actuator-driven jets to hard-tissue cutting was assessed through drilling experiments on porcine femoral condyles, following procedures consistent with earlier bone-jet studies.[38-40] Jets were generated using a 0.5 mm orifice, a 36° nozzle angle, a capacitor charging voltage of 500 V, and a fixed nozzle-to-bone standoff of 1 mm. The setup ensured controlled evaluation of jet-bone interaction under conditions directly comparable with prior investigations.

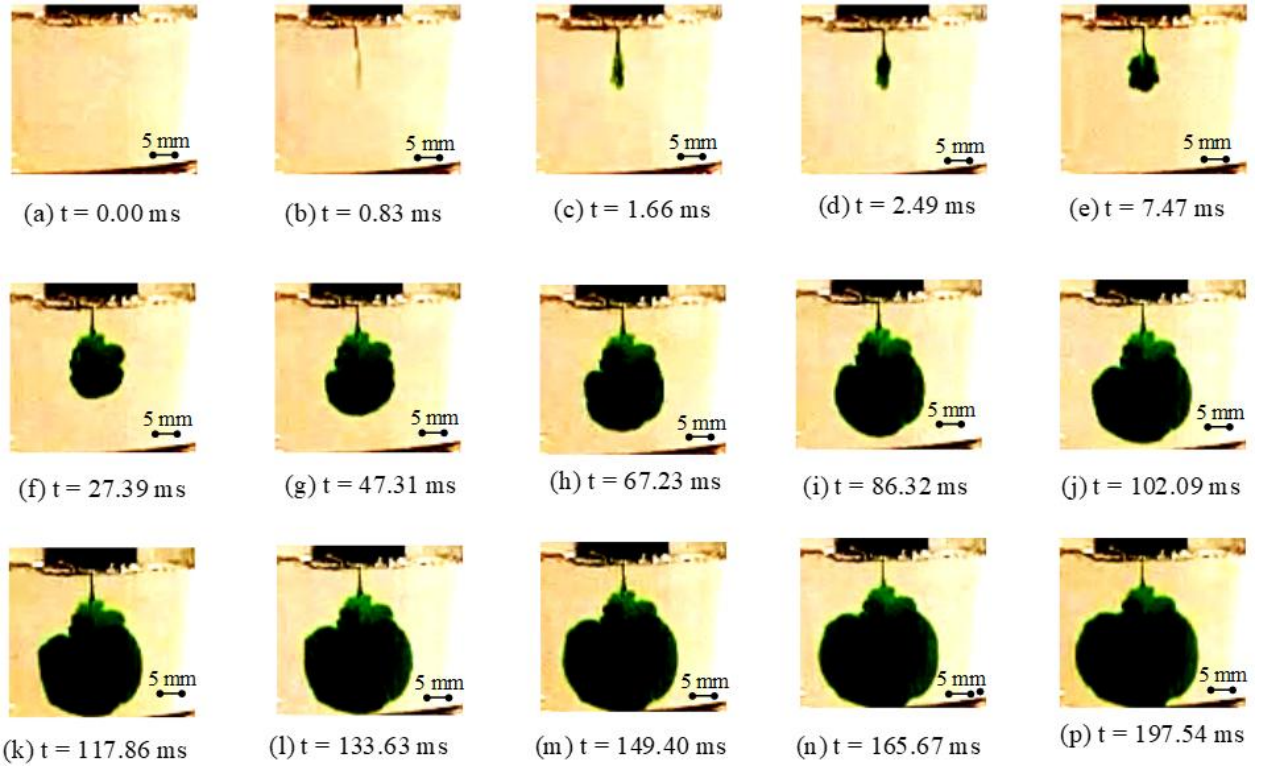

Fig. 13: Temporal evolution of jet penetration in a 20% PAAm gel at 500 V and 0.5 mL.

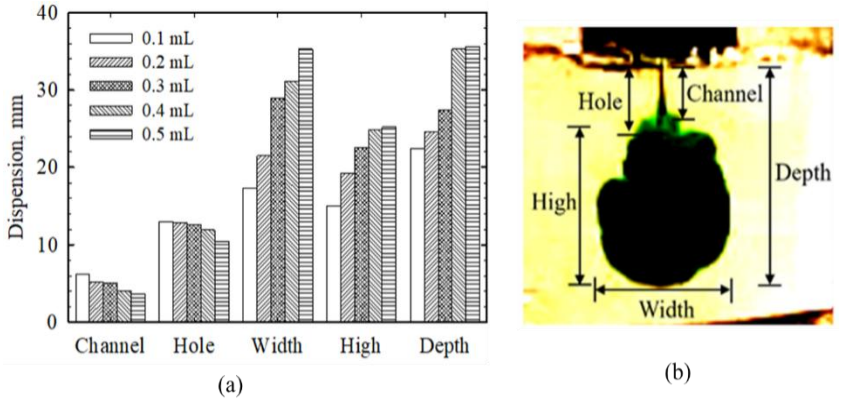

Fig. 14: Dispersion morphology of jets in a 20% PAAm gel for varying liquid volumes: (a) Experimental visualization showing channel, hole, width, height, and depth parameters; the green region represents the methylene-blue-dyed water jet and (b) Quantitative dispersion dimensions (channel, hole, width, height, and depth) for injection volumes of 0.1–0.5 mL.

Fig. 15(a) shows the effect of liquid volume per pulse on drilling depth with pulse number fixed at 20. CT imaging (slice resolution 0.625 mm) confirmed that drilling depth increased with volume, reaching 3.02 mm at 0.5 mL/pulse. This outcome reflects the direct scaling of momentum flux with injected liquid volume, as larger fluid masses impart greater impulse to the bone surface. The result aligns with previous findings that drilling depth correlates with the total momentum delivered per jet impact.[38-40]

In the second series, pulse number was varied while maintaining a fixed volume of 0.5 mL. As shown in Fig. 15(b), drilling depth increased nearly linearly with pulse count, reaching 4.52 mm at 80 pulses. However, the slope of the depth-pulse curve decreased at higher pulse counts, reflecting the transition into denser subchondral layers beneath the articular cartilage that resist further penetration. Importantly, the calculated depth-to-volume efficiency of 0.113 mm/mL was more than double that of conventional waterjet drilling (0.045 mm/mL),[39] demonstrating superior fluid utilization and energy efficiency in the electromagnetic system.

Taken together, these results confirm that electromagnetic actuator-driven jets can achieve precise, controllable, and energy-efficient bone drilling. Compared to conventional waterjet approaches, the present system delivers greater drilling depth with reduced fluid consumption, highlighting its potential as a minimally invasive alternative to mechanical drilling. Beyond biomedical applications, the tunability of jet parameters-including volume, pulse count, and nozzle geometry-offers a flexible engineering framework for optimizing hard-material processing. Future work should

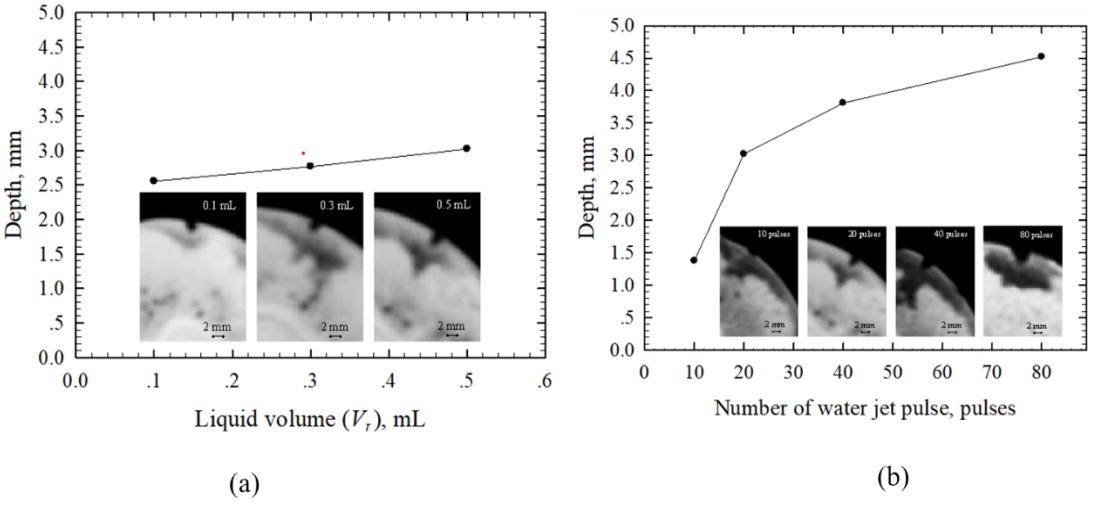

Fig. 15: Results of bone drilling parametric studies: (a) effect of jet volume per pulse on drilling depth at a constant 20 pulses and (b) effect of pulse number on drilling depth at a fixed liquid volume of 0.5 mL.

address clinical translation by refining pulse control, reducing fluid demand, and tailoring operating conditions for surgical integration.

3.5 Implications and limitations

The integrated experimental-CFD framework demonstrated predictive reliability within 10%, enabling virtual optimization of nozzle geometries and operating conditions while reducing prototyping demands. Electromagnetic actuation provided electrical tunability, repeatable pulsatile waveforms, and compact integration, translating into higher depth-to-volume efficiency than conventional waterjets and scalability for portable systems.[13,7-23,31]

Validated across both soft-tissue analogs and bone, the system consistently exceeded NFJI thresholds (>100 m/s, >15 MPa) and achieved drilling depths of 4.52 mm with more than twice the efficiency of traditional methods. Dimensionless scaling (Re, We, and Fr) further established general design rules transferable across fluids, geometries, and scales.

Whether the PAAm gel and porcine bone models provided reproducible and controllable test media, they represent idealized and isotropic approximations of biological tissues. In reality, soft tissues exhibit viscoelastic, nonlinear, and anisotropic mechanical behavior, whereas bone displays structural heterogeneity and directional strength variations. These complexities were beyond the scope of the current validation but will be addressed in future work through viscoelastic constitutive modeling and anatomically realistic digital phantoms. Additionally, limitations of this study include the reliance on PAAm gels and ex vivo bone, the absence of in vivo validation, and unassessed thermal and duty-cycle performance under prolonged use. Future research will therefore focus on heterogeneous and patient-specific tissues, integrating real-time feedback control, energy efficiency assessment, and extending CFD simulations to fully three-dimensional anatomies. Incorporating these aspects will refine CFD-experiment coupling and enhance the translational relevance of electromagnetic jet technology for practical biomedical applications.

Overall, this work positions electromagnetic actuator-driven jets as a unifying platform for both biomedical delivery and precision micromachining, bridging clinical translation and industrial adaptation.

4. Conclusion

This study addressed the limitations of conventional needle-based injections and mechanical drilling by developing and validating an electromagnetic actuator-driven jet system as a controllable and energy-efficient alternative. The approach combined actuator design, high-speed imaging, PVDF sensors, computed tomography/optical coherence tomography (CT/OCT) measurements, and transient CFD modeling with the Volume of Fluid method and SST turbulence closure, creating an integrated experimental–computational framework for jet characterization. The system consistently produced high-speed jets suitable for biomedical applications. In soft-tissue analogs, jets exceeded the NFJI threshold with velocities above 100 m/s and impact pressures greater than 20 MPa, achieving penetration depths over 40 mm and dispersion widths of around 30 mm. CFD predictions matched experimental results within 10%, confirming the robustness of the framework. In bone drilling tests, depths of 4.52 mm were obtained with a depth-to-volume efficiency of 0.113 mm/mL, more than double the efficiency of conventional waterjet drilling (0.045 mm/mL). Dimensionless scaling further verified inertia-dominated, turbulence-controlled jet behavior. While these results confirm the system's technical feasibility and promise, this work represents an early-stage validation rather than a clinically or industrially deployable solution. Further investigations on in vivo safety, long-term durability, and large-scale manufacturing are required. Overall, the study establishes foundational evidence supporting electromagnetic needle-free jet technology as a viable direction for future advancements in biomedical, veterinary, and precision

engineering applications.

Acknowledgments
The authors gratefully acknowledge the financial support provided by Ubon Ratchathani University through the Fundamental Fund 2024 (Project No. 198338) and by the Thailand Research Fund (TRF) under Contract No. RSA5780001. The authors also wish to thank the College of Medicine and Public Health, Ubon Ratchathani University, for providing CT/OCT imaging facilities.

Conflict of Interest
The authors declare no conflict of interest**.**

Supporting Information
Not applicable.

CRediT Statement
Sumeta Sribun: Investigation, Methodology, Data curation, Formal analysis, Visualization, Software. **Anirut Matthujak:** Conceptualization, Methodology, Validation, Supervision, Writing – Original draft, Writing - Review & editing, Funding acquisition. **Gittiphong Sripanagul:** Investigation, Methodology, Data curation, Formal analysis. **Thanarath Sriveerakul:** Supervision, Validation, Formal analysis, Visualization. **Jinda Glinubon:** Investigation, Methodology, Data curation, Formal analysis, Visualization. **Sutthisak Phongthanapanich:** Supervision, Validation, Writing - Review & editing.

References
[1] G. Sripanagul, A. Matthujak, T. Sriveerakul, S. Phongthanapanich, Experimental investigation of stone drilling using water jet generated by electromagnetic actuator, *International Journal of Rock Mechanics and Mining Sciences*, 2021, **142**, 104697, doi: 10.1016/j.ijrmms.2021.104697.
[2] T. Yang, W. Zhao, X. Zhu, Morphological study of cortical bone damage caused by high-pressure water jet erosion based on SPH-FEM coupling algorithm, *Journal of Manufacturing Processes*, 2024, **118**, 195-205, doi: 10.1016/j.jmapro.2024.03.044.
[3] J. Kurian, Harnessing Aerospace Fluid Mechanics and Cavitation for Biomedical Engineering: Advancing Non-Invasive Therapies, Drug Delivery, and Medical Devices, *Regional Student Conferences*, Reston, Virginia, 2025, 98728, doi: 10.2514/6.2025-98728.
[4] J. M. Rosselló, C. D. Ohl, Bullet jet as a tool for soft matter piercing and needle-free liquid injection, *Biomedical Optics Express*, 2022, **13**(10), 5202–5216, doi: 10.1364/boe.469486.
[5] X.-F. Song, J. Zhao, H. Yan, W. Yu, L. Yin, Waterjet machining of biological tissues in medical surgeries: From soft tissue dissection to bone cutting, *Journal of Manufacturing Processes*, 2023, **107**, 529-548, doi: 10.1016/j.jmapro.2023.10.067.
[6] A. Nag, S. Hloch, A. R. Dixit, F. Pude, Utilization of ultrasonically forced pulsating water jet decaying for bone cement removal, *The International Journal of Advanced Manufacturing Technology*, 2020, **110**, 829-840, doi: 10.1007/s00170-020-05892-9.
[7] M. A. Trimzi, Y. B. Ham, A needle-free jet injection system for controlled release and repeated biopharmaceutical delivery, *Pharmaceutics*, 2021, **13**, 1770, doi: 10.3390/pharmaceutics13111770.
[8] H. Nakayama, R. Portaro, C. B. Kiyanda, H. D. Ng, Cfd modeling of high speed liquid jets from an air-powered needle-free injection system, *Journal of Mechanics in Medicine and Biology*, 2016, **16**, 1650045, doi: 10.1142/s0219519416500457.
[9] A. Taberner, N. C. Hogan, I. W. Hunter, Needle-free jet injection using real-time controlled linear Lorentz-force actuators, *Medical Engineering & Physics*, 2012, **34**, 1228-1235, doi: 10.1016/j.medengphy.2011.12.010.
[10] J. W. McKeage, A. Z. H. Tan, A. J. Taberner, Large volume subcutaneous delivery using multi-orifice jet injection, *International Journal of Pharmaceutics*, 2024, **649**, 123605, doi: 10.1016/j.ijpharm.2023.123605.
[11] Y. Zhu, C. Kang, W. Cai, C. Huang, Drug injection and dispersion characteristics of an air-powered needle-free injector, *Medical Engineering & Physics*, 2022, **109**, 103906, doi: 10.1016/j.medengphy.2022.103906.
[12] A. Mohizin, J. K. Kim, Conceptualisation of a novel electromechanical system for small-volume needle-free jet injection, *Engineering Applications of Computational Fluid Mechanics*, 2023, **17**, doi: 10.1080/19942060.2023.2240868.
[13] D. Zeng, N. Wu, L. Qian, H. Shi, Y. Kang, A novel controllable pneumatic needle-free injection system for larger-volume drug delivery, *Journal of Pharmaceutical Sciences*, 2020, **109**, 1772-1779, doi: 10.1016/j.xphs.2020.02.003.
[14] Y. Lu, S. Zhang, F. He, L. Wang, A. Wang, M. Wang, Experimental and numerical simulation study on the relationship between cutting depth of high-pressure water jet with high traverse speed and disc cutter penetration of TBM in hard rock tunnel, *Tunnelling and Underground Space Technology*, 2023, **142**, 105387, doi: 10.1016/j.tust.2023.105387.
[15] A. Matthujak, K. Pianthong, K. Takayama, B. E. Milton, Experimental study of ignition over impact-driven supersonic liquid fuel jet, *Advances in Mechanical Engineering*, 2013, **2013**, 928970, doi: 10.1155/2013/928970.
[16] A. Matthujak, C. Kasamnimitporn, T. Sriveerakul, Comparative visualized investigation of impact-driven high-speed liquid jets injected in submerged water and in ambient air, *Journal of Visualization*, 2020, **23**, 395-408, doi: 10.1007/s12650-020-00640-3.
[17] A. Matthujak, S. H. R. Hosseini, K. Takayama, M. Sun, P. Voinovich, High speed jet formation by impact acceleration method, *Shock Waves*, 2007, **16**, 405-419, doi: 10.1007/s00193-007-0079-9.
[18] A. Matthujak, C. Kasamnimitporn, W. Sittiwong, K. Pianthong, K. Takayama, B. E. Milton, Characteristics of impact-driven high-speed liquid jets in water, *Shock Waves*, 2013, **23**, 105-114, doi: 10.1007/s00193-013-0431-1.

[19] J. C. Stachowiak, M. G. von Muhlen, T. H. Li, L. Jalilian, S. H. Parekh, D. A. Fletcher, Piezoelectric control of needle-free transdermal drug delivery, *Journal of Controlled Release*, 2007, **124**, 88-97, doi: 10.1016/j.jconrel.2007.08.017.
[20] K. Li, J.-K. Liu, R. Yang, W.-S. Chen, L. Zhang, The numerical and experimental research on injection performance of piezoelectric micro-jet, *Ceramics International*, 2017, **43**, S27-S35, doi: 10.1016/j.ceramint.2017.05.200.
[21] L. Zhang, Z. Gan, S. Liu, X. Zhang, N. Yang, H. Wang, Q. Zhang, X. Liu, K. Wang, J. Liu, Effects of piezoelectric synthetic jet actuator parameters on synthetic jet formation process and actuator performance, *International Journal of Non-Linear Mechanics*, 2023, **157**, 104561, doi: 10.1016/j.ijnonlinmec.2023.104561.
[22] J. H. Chang, N. C. Hogan, I. W. Hunter, A needle-free technique for interstitial fluid sample acquisition using a Lorentz-force actuated jet injector, *Journal of Controlled Release*, 2015, **211**, 37-43, doi: 10.1016/j.jconrel.2015.05.264.
[23] T. Dong, Z. Ban, S. Zheng, Y. Gu, T. Liu, Enhanced actuation performance in liquid metal electromagnetic actuators with optimized microchannel for soft robotic applications, *Sensors and Actuators A: Physical*, 2025, **393**, 116842, doi: 10.1016/j.sna.2025.116842.
[24] J. Lee, S. Park, D. Yoon, C. Murugan, S. Bang, S. Park, Targeted drug delivery using self-unrolling sheets in magnetically actuated capsules, *Device A Cell Press Journal*, 2025, **3**, 100654, doi: 10.1016/j.device.2024.100654.
[25] S. H. Lee, B. H. Kim, C. G. Park, C. Lee, B. Y. Lim, Y. B. Choy, Implantable small device enabled with magnetic actuation for on-demand and pulsatile drug delivery, *Journal of Controlled Release*, 2018, **286**, 224-230, doi: 10.1016/j.jconrel.2018.07.037.
[26] V. Sant, L. Wang, G. Jang, D. Ban, J. Seth, S. Kazmi, N. R. Patel, Q. Yang, J. Lee, W. Janetanakit, S. Wang, B. Head, G. Glinsky, R. Lal, Nanocarriers for magnetically actuated targeted drug delivery, *Biophysical Journal*, 2019, **116**, 33a, doi: 10.1016/j.bpj.2018.11.220.
[27] S. Khotthada, A. Matthujak, P. Khamphakdi, J. Glinubon, C. Siriboon, I. Salangam, S. Phongthanapanich, Development and performance analysis of an electromagnetic needle-free jet injection device for efficient drug delivery in pig farms, *Engineered Science*, 2024, **33**, 1329, doi: 10.30919/es1329.
[28] Z. Wang, D. Song, J. Wang, L. Xiong, T. Shi, C. Zhang, L. Di, C. Zhang, Y. Zhang, H. Li, X. Liu, J. Liu, Y. Zhang, Simulation and experimental study on the influence of needle-free jet injection nozzle structure on injection performance, *Journal of Drug Delivery Science and Technology*, 2022, **68**, 103043, doi: 10.1016/j.jddst.2021.103043.
[29] A. Mohizin, J. K. Kim, Current engineering and clinical aspects of needle-free injectors: a review, *Journal of Mechanical Science and Technology*, 2018, **32**, 5737-5747, doi: 10.1007/s12206-018-1121-9.
[30] A. Issakhov, A. Sabyrkulova, A. Abylkassymova, CFD modeling the disintegration of an intranasal spray jet in the human upper respiratory tract using the VOF-to-DPM model, *Communications in Nonlinear Science and Numerical Simulation*, 2025, **151**, 109093, doi: 10.1016/j.cnsns.2025.109093.
[31] G. Sripanagul, A. Matthujak, Fundamental study of electromagnetic actuated needle-free jet injection, *International Journal of Engineering & Technology*, 2018, **7**, 145-148, doi: 10.14419/ijet.v7i3.7.16258.
[32] A. Mohizin, K. E. Reby Roy, D. Lee, S. K. Lee, J. K. Kim, Computational fluid dynamics of impinging microjet for a needle-free skin scar treatment system, *Computers in Biology and Medicine*, 2018, **101**, 61-69, doi: 10.1016/j.compbiomed.2018.08.005.
[33] A. S. Grinspan, R. Gnanamoorthy, Impact resistance of liquid jet impingement on polymers, *Materials & Design*, 2010, **31**, 4638–4645, doi: 10.1016/j.matdes.2010.05.034.
[34] A. B. Gojani, H. Obara, K. Okada, K. Takayama, Impact pressure measurement using a PVDF film sensor in a water jet, *Review of Scientific Instruments*, 2016, **87**, 025118, doi: 10.1063/1.4942100.
[35] J. Schramm-Baxter, J. Katrencik, S. Mitragotri, Jet injection into polyacrylamide gels: investigation of jet injection mechanics, *Journal of Biomechanics*, 2004, **37**, 1181-1188, doi: 10.1016/j.jbiomech.2003.12.006.
[36] O. A. Shergold, N. A. Fleck, D. Radford, The uniaxial stress versus strain response of pig skin and silicone rubber at low and high strain rates, *International Journal of Impact Engineering*, 2006, **32**, 1384-1402, doi: 10.1016/j.ijimpeng.2004.11.010.
[37] Y.-C. Wang, Y.-W. Chen, Application of piezoelectric PVDF film to the measurement of impulsive forces generated by cavitation bubble collapse near a solid boundary, *Experimental Thermal and Fluid Science*, 2007, **32**, 403-414, doi: 10.1016/j.expthermflusci.2007.05.003.
[38] S. den Dunnen, L. Mulder, G. M. M. J. Kerkhoffs, J. Dankelman, G. J. M. Tuijthof, Waterjet drilling in porcine bone: the effect of the nozzle diameter and bone architecture on the hole dimensions, *Journal of the Mechanical Behavior of Biomedical Materials*, 2013, **27**, 84-93, doi: 10.1016/j.jmbbm.2013.06.012.
[39] S. den Dunnen, G. J. M. Tuijthof, The influence of water jet diameter and bone structural properties on the efficiency of pure water jet drilling in porcine bone, *Mechanical Sciences*, 2014, **5**, 53-58, doi: 10.5194/ms-5-53-2014
[40] S. den Dunnen, J. Dankelman, G. M. M. J. Kerkhoffs, G. J. M. Tuijthof, How do jet time, pressure and bone volume fraction influence the drilling depth when waterjet drilling in porcine bone? *Journal of the Mechanical Behavior of Biomedical Materials*, 2016, **62**, 495-503, doi: 10.1016/j.jmbbm.2016.05.030.